Scattering-free edge states between heterogeneous photonic topological insulators

Tzuhsuan Ma[1] and Gennady Shvets[2,*]

[1]*Department of Physics, The University of Texas at Austin, Austin, Texas 78712, USA*

[2]*School of Applied and Engineering Physics, Cornell University, Ithaca, New York 14853, USA*

(Received 17 July 2015; published 3 April 2017)

We propose a set of three compatible photonic structures emulating quantum topologically insulating phases corresponding to Hall, spin-Hall, and valley-Hall effects. It is shown that an interface between any two of these photonic topological insulators supports scattering-free edge states. Spin and valley degrees of freedom characterizing such topologically protected edge waves determine their unique pathways through complex photonic circuits comprised of multiple heterogeneous interfaces.

DOI: 10.1103/PhysRevB.95.165102

I. INTRODUCTION AND MOTIVATION

Light propagation through photonic crystals, metamaterials, and other guiding structures can often be reduced to a simple scalar wave equation that imposes fundamental limitations on how electromagnetic energy can be transported through space. For example, reflectionless guiding of light along sharply bent trajectories without reflections is generally believed to be impossible. This conventional wisdom has been recently been overturned with the realization of a new class of photonic structures: photonic topological insulators (PTIs) [1–13]. Just as their condensed matter counterparts, topological insulators (TIs) [14–17] from which they have been derived by analogy, PTIs enable reflection-free propagation of topologically protected edge waves (TPEWs) [8,11,18,19] along almost arbitrarily shaped domain walls separating the PTIs with different topological indices. The three basic condensed matter systems supporting topological insulating phases—quantum Hall (QH) [20,21], quantum spin-Hall (QSH) [14–16], and quantum valley-Hall (QVH) [22–27] TIs—have all been emulated in photonics.

However, the challenges in integrating heterogeneous materials prevented experimentalists from realizing the domain walls separating *different TI classes* (e.g., QSH and QH) despite recent theoretical [28] proposals. In this paper, we construct an electromagnetic equivalent of such interfaces supporting TPEWs. It is shown that the conservation of two discrete photonic degrees of freedom (DOF), the spin [7,8,11], and the *valley* [29], enables TPEWs, despite the absence of globally defined topological indices [30–32]. Moreover, because the three photonic structures introduced below share the same platform (see Figs. 1 and 2), they can be easily embedded inside each other. We utilize such integration to propose several exotic physical phenomena that occur when an island comprised of one PTI type is embedded inside another one containing a TPEW-supporting domain wall [26,31,32].

The specific new effects are as follows: (a) nonreciprocal and (b) valley-dependent scattering of spin-polarized chiral edge states taking place when the island is comprised, respectively, of a QH or QVH insulating phase. The effect (a), which lends itself to the development of broadband nonreciprocal devices [33,34], relies on the existence of one-way TPEWs between two PTIs, only one of which has a globally defined topological index. The effect (b), which amounts to valley-filtering of spin-polarized edge states, relies on the simultaneous preservation of the spin and valley DOFs that enables TPEWs at the domain wall between PTIs with valley- and spin-dependent topological indices. Note that edge states between PTIs and topologically trivial media are outside of the scope of this paper because they do not offer the same functionalities as the TPEWs between different PTIs.

The rest of the paper is organized as follows. The connection between electronic and photonic topological phases is briefly reviewed in Sec. II. The three photonic topological insulating phases corresponding to QH, spin-Hall, and QVH effects are introduced in Sec. III using a common photonic platform. We refer to the photonic structures that support such topologically insulating phases as QH-PTIs, QSH-PTIs, and QVH-PTIs. Examples of all three types of PTIs obtained using first-principles electromagnetics simulation are presented, with special emphasis on symmetry breaking perturbations that enable the three phases. The effective Hamiltonians describing wave propagation in such structures are derived, and the corresponding topological indices such as the global Chern, valley-Chern, and spin-Chern numbers, are obtained. These topological indices are then used in Sec. IV to derive the properties of the TPEWs that emerge at the interface between heterogeneous PTIs, e.g., between a QH-PTI and a QSH-PTI, or between a QVH-PTI and a QSH-PTI. An example of robust propagation of such TPEWs through a disordered region is presented in Sec. V. An example of valley sorting of TPEWs that can be achieved by embedding a QVH-PTI island inside a sea of QSH-PTIs containing a domain wall is presented in Sec. VI. An example of a four-port broadband circulator based on nonreciprocal TPEWs between QSH-PTIs and a QVH-PTI is analyzed in Sec. VII. Conclusions and outlook are presented in Sec. VIII.

II. RELATION TO ELECTRONIC TOPOLOGICAL PHASES

Before analyzing the electromagnetic properties of the PTIs, we briefly introduce the main ingredients and physical principles that enable accurate mapping between electronic and photonic topological phases. Conceptually, the three types of graphenelike two-dimensional (2D) electronic TIs can be constructed by perturbing the electronic states of graphene near the high-symmetry points of the Brillouin zone (BZ)

*gshvets@cornell.edu

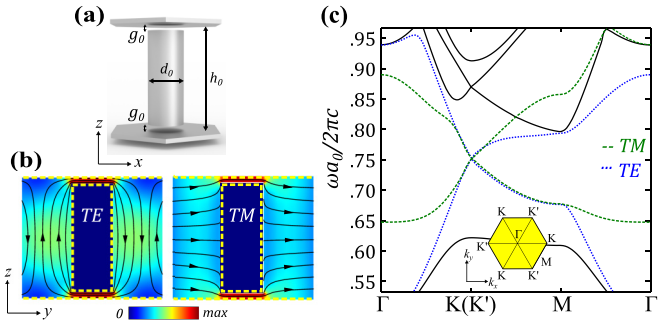

FIG. 1. The unperturbed PhG structure used for emulating photon equivalents of the spin and valley degrees of freedom. (a) The unit cell of the PhG: metal rods arranged as a hexagonal array lattice with the lattice constant a_0. (b) Magnetic field profiles of the TE and TM modes at the K point. (c) The photonic band structure with TE and TM modes forming doubly-degenerate Dirac cones at $K(K')$ points. Design parameters: $h_0 = a_0$, $d_0 = 0.345a_0$, and $g_0 = 0.05a_0$.

where the valence and conduction bands coalesce to form Dirac cones. For example, QH-TIs are produced by a magnetic field that breaks the time-reversal (T) symmetry. The resulting interaction with the orbital DOF is spin-independent. On the other hand, the perturbation responsible for the emergence of a QSH-TI takes the form of the Kane-Mele [14] spin-orbit coupling (SOC) that directly involves the spin DOF.

Finally, a QVH-TI emerges from the spin-independent perturbations that break the in-plane parity (P) symmetry, e.g., in AB-BA stacked electrically biased bilayer graphene [26,32,35], in graphene placed on top of hexagonal boron nitride [27], or in other 2D materials with broken inversion symmetry such as, for example, MoS_2 and other group-VI dichalcogenides [36,37]. Just as the magnetic field lifts the degeneracy between the orbital states in QSH systems, so does the above P-symmetry breaking perturbation, albeit without breaking the T-symmetry. Such spin-independent perturbation produces a bandgap by lifting the degeneracy between the orbital states in the K and K' valleys of the BZ. While physical magnetic fields and their associated real-space vector potentials are required for the QH phase, their momentum-space analogs known as the Berry curvature and Berry connection are responsible for the QSH and QVH phases [20,38,39].

Each of these perturbations opens a bandgap in the K and K' valleys of the BZ and endows their respective topological phases with nontrivial topological Chern numbers: global for QH-TIs [20,21], spin-connected for QSH-TIs [14], and valley-connected [40] for QVH-TIs. The emergence of the bandgap-crossing conducting edge states at the domain walls between TIs with different Chern numbers according to the bulk-boundary correspondence [28,41,42] is a fundamental property of electronic topological phases that is highly desirable to emulate in photonics. Of course, the physical meaning of the edge states in photonics is very different than in condensed matter physics. The edge states (which we will be referring to as edge waves from this point on) represent electromagnetic oscillations that are evanescent on both sides of the domain wall. They can be launched, for example, using single [18] or multiple [43] dipole antennas.

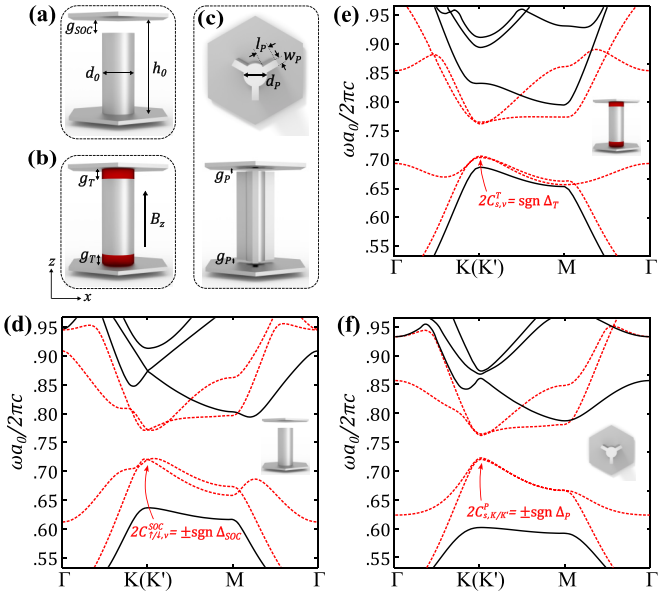

FIG. 2. A library of topological phases of light. (a)–(c) The unit cells of the three PTIs emulating QSH, QH, and QVH effects, respectively. (b) The gyromagnetic material (red disks) has the following constitutive parameters: $\epsilon = 1$, $\mu_{xx/yy/zz} = 1$, $\mu_{xy} = -\mu_{yx} = -i\delta$ with $\delta = 0.8$, and $\mu_{ij} = 0$ otherwise. (d)–(f) Photonic band structures corresponding to the PTIs in (a)–(c), respectively. The bandgap widths Δ are proportional to the respective overlap integrals $\Delta_{\rm SOC} \propto g_{\rm SOC}$, $\Delta_T \propto \delta \times g_{\rm T}$, and Δ_P defined in SM. The local spin-valley Chern indices of the lower bands are listed. Geometric parameters are chosen to ensure spin-degeneracy and approximately equal band gaps: $h_0 = a_0$, $d_0 = 0.345a_0$, $g_{\rm SOC} = 0.15a_0$, $g_{\rm T} = 0.1a_0$, $g_{\rm P} = 0.03a_0$, $d_P = 0.2a_0$, $l_P = 0.116a_0$, and $w_P = 0.06a_0$. The symmetric rod-to-plate gaps in (c) can be filled with low-index spacers for structural stability.

III. THEORETICAL DESCRIPTION OF THE THREE PHOTONIC TOPOLOGICAL PHASES

The photonic analogues of the three topological phases are obtained by imposing three types of distinct symmetry-breaking perturbations on a simple symmetric photonic graphene (PhG) [44] platform shown in Fig. 1(a). The PhG is comprised of a hexagonal array of metal posts symmetrically placed between the two confining metal plates and separated from them by the gap g_0. A similar photonic structure was considered earlier in the narrower context of QSH-type [11] PTIs. The PhG structure supports the transverse electric (TE) and transverse magnetic (TM) modes, shown in Fig. 1(b), that are intentionally designed to be degenerate [see the bands' crossing at the Dirac frequency $\omega_D \approx 0.75 \times 2\pi c/a_0$ in Fig. 1(c)] at the $K(K')$ corners of the BZ. Such degeneracy is required for emulating the spin DOF associated with the phase difference [7,11] between these key expansion modes. The Dirac point crossings in the band structure of the PhG are fragile and are destroyed by a broad class of perturbations that create a bandgap where the Dirac crossing used to be. Electromagnetic waves propagating in the resulting gapped PhG can, in fact, have topological properties that are very similar to those of the electrons in gapped graphene. Such gapped topological structures (PTIs) emerge under a subclass

of perturbations that preserve various discrete DOF such as, for example, the synthetic spin DOF [7,8,11,13,18,19] and the valley DOF [29]. Such perturbations, analytically described below and sketched in Fig. 2, enable topological phases of light that are mathematically equivalent to their quantum counterparts from condensed matter physics.

A. Summary of the results

Guided by the symmetries-based analogy between electronic and photonic TIs, we now present in Figs. 2(a)–2(c) the three perturbations of the PhG emulating the QSH/QH/QVH topological phases. Their equivalence with the corresponding 2D quantum electronic phases is mathematically established below by applying the Slater perturbation theory [45,46] under the four-mode (twice-degenerate TE/TM) approximation. The calculations of the corresponding normalized band gaps $\Delta_{\mathrm{SOC}}/\Delta_T/\Delta_P$, as well as of the Chern numbers of the propagating electromagnetic modes spectrally located below the band gap, are presented below. Note a key distinction between the physical spin-1/2 of an electron and the synthetic spin DOF of a photon: The former is strictly conserved under T-symmetric (nonmagnetic) lattice defects, while the latter is preserved under a restricted set of perturbations [11,18,19]. Further, spin conservation in a photonic structure depends on the accuracy of the four-mode approximation that requires that no other electromagnetic modes contribute to the expansion of the perturbed electromagnetic fields.

The bianisotropic symmetry breaking emulating the SOC [11] consists of filling one of the rod-to-plate gaps with metal as illustrated in Fig. 2(a). It results in the spectral gap opening near the Dirac points as shown in Fig. 2(d), with the bandgap proportional to the overlap integral Δ_{SOC} between the TE/TM modes inside the metal-to-plate gap. The electromagnetic modes propagating above and below the bandgap have a QSH-like topological nature, with the spin-Chern number given by $2C^{\mathrm{SOC}}_{\uparrow/\downarrow,v} = \pm 1 \times \mathrm{sgn}(\Delta_{\mathrm{SOC}})$, where $s = \uparrow, \downarrow$ is the spin state label, $v = K, K'$ is the valley label, and the valley-independent $\Delta_{\mathrm{SOC}} > 0$ ($\Delta_{\mathrm{SOC}} < 0$) if the top (bottom) gaps are filled with metal. For the frequencies inside the bandgap, this structure behaves as a QSH-PTI.

Likewise, a deformation to tripodlike C_3-symmetric metallic shapes shown in Fig. 2(c) that breaks the mirror-reflection symmetry (P-inversion) with respect to the principal translation axes of the lattice gives rise to the bandgap opening shown in Fig. 2(f). The rotation symmetry of the tripod is essential for the decoupling and degeneracy of the two valleys. When the perturbations of the TE and TM modes are matched, the structure becomes a QVH-PTI inside the bandgap, with a spin-independent valley-Chern number $2C^{P}_{s,K/K'} = \pm 1 \times \mathrm{sgn}(\Delta_P)$ of the propagating electromagnetic waves [29] below the bandgap. The global Chern numbers of both structures shown in Figs. 2(a) and 2(c) vanish due to the T-symmetry: $\sum_{s,v} C^{P}_{s,v} = \sum_{s,v} C^{\mathrm{SOC}}_{s,v} = 0$.

Finally, the spin- and valley-independent QH-PTI is emulated by inserting magnetized gyromagnetic material into the two gaps, as shown in Fig. 2(b). The magnetic permittivity tensor is assumed in the form of $\mu_{xx/yy/zz} = 1, \mu_{xy} = -\mu_{yx} = -i\delta$, and $\mu_{ij} = 0$ otherwise. The propagating modes plotted in Fig. 2(e) represent a photonic QH-like topological phase characterized by a global Chern number $2C^{T}_{s,v} = \mathrm{sgn}(\Delta_T)$, where Δ_T is linearly proportional to δ, as well as to the field overlap integral (see SM) inside the gyromagnetic region. Unlike earlier zero-spin (single-mode) QH-PTI concepts [1–3], our approach encompasses the spin DOF while ensuring that the electromagnetic waves propagation is both spin- and valley-independent. This property enables nonreciprocal TPEWs at the interface between QH-PTIs and the QSH-/QVH-PTIs, thus greatly expanding the library of photonic architectures.

After stating the properties of the three photonic topological phases, we now sketch out the mathematical analogy between the three topological photonic phases in the perturbed PhG and their 2D quantum electronic counterparts. This analogy enables us to formulate the low energy effective Hamiltonian for the electromagnetic waves that are propagating close to the Dirac degeneracy point corresponding to the K/K' corners of the BZ. The effective Hamiltonian $\mathcal{H}(\boldsymbol{k}_\perp)$, which is a function of the Bloch wave number $\boldsymbol{k}_\perp$, is derived in the limit of small $\delta\boldsymbol{k} \equiv \boldsymbol{k}_\perp - \boldsymbol{K}$ (where $\boldsymbol{K} = \boldsymbol{e}_x 4\pi/3a_0$) or small $\delta\boldsymbol{k}' \equiv \boldsymbol{k}_\perp - \boldsymbol{K}'$ (where $\boldsymbol{K}' = -\boldsymbol{e}_x 4\pi/3a_0$). It acts on an eight-component state vector of a photon that encompasses two orbital DOF [right-hand circular polarizations (RCPs) and left-hand circular polarizations (LCPs)], two synthetic spin DOF (spin-up and spin-down corresponding to in-phase and out-of-phase linear combinations of the TE and TM modes), and two valley DOF (corresponding to the Bloch wave number $\boldsymbol{k}_\perp$ being close to either $\boldsymbol{K}$ or $\boldsymbol{K}'$ nonequivalent corners of the BZ).

We then use the effective Hamiltonian for the following purposes: (a) to calculate the corresponding topological Chern numbers for each phase (b) to apply the bulk-boundary correspondence principle and to derive the properties of the edge states propagating at the interface between different topological phases. Thus, these heterogeneous PTIs form a set of topological claddings supporting the localized edge states. The edge states are spectrally located inside the bandgap separating topological phases with different Chern numbers in each of the topological claddings. They are topologically protected under a well-defined set of lattice defects that preserve the spin and valley DOF.

B. Dirac dispersion and the effective Hamiltonian of the unperturbed PhG

The lowest order mutually orthogonal eigenmodes of the PhG shown in Fig. 1(a) are classified as TM- and TE-like based on their field profiles shown in Fig. 1(b). Because only the lowest order TE and TM modes exist in the K and K' valleys, any electromagnetic mode with the Bloch wavenumber $\boldsymbol{k}_\perp$ can be expanded as

$$\boldsymbol{E}(\boldsymbol{r},t) = \sum_{n,\boldsymbol{k}_\perp} \left[a_e^n(\boldsymbol{k}_\perp)\boldsymbol{e}_e^{n,\boldsymbol{k}_\perp}(\boldsymbol{r}_\perp,z) + a_m^n(\boldsymbol{k}_\perp)\boldsymbol{e}_m^{n,\boldsymbol{k}_\perp}(\boldsymbol{r}_\perp,z)\right] \times e^{i\boldsymbol{k}_\perp\cdot\boldsymbol{r}_\perp - i\omega_n(\boldsymbol{k}_\perp)t} + \mathrm{c.c.} \quad (1)$$

$$\boldsymbol{H}(\boldsymbol{r},t) = \sum_{n,\boldsymbol{k}_\perp} \left[a_e^n(\boldsymbol{k}_\perp)\boldsymbol{h}_e^{n,\boldsymbol{k}_\perp}(\boldsymbol{r}_\perp,z) + a_m^n(\boldsymbol{k}_\perp)\boldsymbol{h}_m^{n,\boldsymbol{k}_\perp}(\boldsymbol{r}_\perp,z)\right] \times e^{i\boldsymbol{k}_\perp\cdot\boldsymbol{r}_\perp - i\omega_n(\boldsymbol{k}_\perp)t} + \mathrm{c.c.}, \quad (2)$$

where the $n = 1,2$ index refers to lower (upper) propagation bands and $\boldsymbol{e}_e^{n,\boldsymbol{k}_\perp}$, $\boldsymbol{h}_e^{n,\boldsymbol{k}_\perp}$, $\boldsymbol{e}_m^{n,\boldsymbol{k}_\perp}$, and $\boldsymbol{h}_m^{n,\boldsymbol{k}_\perp}$ are the normalized field profiles chosen to be periodic in the $\boldsymbol{r}_\perp = (x,y)$ plane. The TE/TM-like modes, labeled as e/m, are defined by the parity of $\hat{\boldsymbol{z}} \cdot \boldsymbol{h}_{e/m}$ with respect z, as illustrated in Fig. 1(b). The eigenfrequencies $\omega_n(\boldsymbol{k}_\perp)$ of the two modes were calculated as functions of the Bloch wavenumber $\boldsymbol{k}_\perp = (k_x,k_y)$ inside the BZ using COMSOL Multiphysics code for a specific PhG with a lattice constant a_0, interplate distance h_0, cylinders' diameter d_0, and the gap size g_0 (see caption for their values).

The resulting dispersion curves are plotted in Fig. 1(c) as dashed (TM) and dotted (TE) lines along with the higher order (solid lines) modes neglected in this paper. The C_{3v} wave vector symmetry group [47] results in doubly degenerate modes at the K/K' edges of the BZ [shown in Fig. 1(c)]. Each mode forms its own Dirac cone in the nonequivalent valleys [22,23,25] of K and K' centered at the respective Dirac frequency $\omega_D^{e,m}$. This degeneracy enables the choice of eigenmodes that have the RCP or LCP in the midplane ($z = h_0/2$), thereby imparting both TE and TM waves with an orbital DOF. Therefore, at the K/K' edges, we choose $n = 1,2$ in Eqs. (1) and (2) to represent the LCP and RCP orbital states, respectively. Moreover, by a judicious choice of h_0, d_0, and g_0, it is possible to achieve the intermode degeneracy [7,11], i.e., $\omega_D^e = \omega_D^m \equiv \omega_D$ and $\partial\omega_D^e/\partial k = \partial\omega_D^m/\partial k \equiv v_D$, as shown in Fig. 1(c). For simplicity, we first concentrate on the K-valley of the BZ, where a finite $\delta\boldsymbol{k} \equiv \boldsymbol{k}_\perp - \boldsymbol{K}$ (where $\boldsymbol{K} = \boldsymbol{e}_x 4\pi/3a_0$) lifts the Dirac degeneracy. The effective K-valley Hamiltonian [29] expressed in the RCP/LCP (orbital) basis is $\mathcal{H}_{0K}^{e,m}(\delta\boldsymbol{k}) = v_D(\delta k_x\hat{\sigma}_x + \delta k_y\hat{\sigma}_y)$, where $\hat{\sigma}_{x,y,z}$ are the Pauli matrices acting on the orbital state vector $\mathbf{U}_K^{e,m} = [a_{e,m}^R; a_{e,m}^L]$. The degenerate expansion basis $\mathbf{U}_R = [1;0]$ and $\mathbf{U}_L = [0;1]$ is defined according to its transformation with respect to the $2\pi/3$ rotation $\mathcal{R}_3$, according to $\mathcal{R}_3\mathbf{U}_{R,L} = \exp(\mp 2\pi i/3)\mathbf{U}_{R,L}$.

Taking advantage of the assumed degeneracy of the TE and TM modes (which is achieved by design in close spectral proximity of $\omega = \omega_D$, as explained above), we can expand the basis states from separate two-component vectors $\mathbf{U}_K^{e,m} = [a_{e,m}^R; a_{e,m}^L]$ to a four-component vector $\boldsymbol{V}_K = \mathbf{M}[\mathbf{U}_K^e; \mathbf{U}_K^m]$, where $\mathbf{M}$ is an arbitrary unitary 4×4 polarization-coupling matrix that does not mix the orbital states while coupling the TE/TM states. We will use $\mathbf{M} = \frac{1}{\sqrt{2}}\begin{pmatrix}1 & 1\\ 1 & -1\end{pmatrix} \otimes \begin{pmatrix}1 & 0\\ 0 & 1\end{pmatrix}$ that transforms from the TE/TM basis to the spin-up/spin-down ($\uparrow$ / $\downarrow$) basis. The significance of the spin basis [7,8,11] is that it diagonalizes the bianisotropic perturbation shown in Fig. 2(a), which, unlike the perturbations shown in Figs. 2(b) and 2(c), directly couples the TE and TM states. Because of the degeneracy of the spin states, the separate unperturbed Hamiltonians $\mathcal{H}_{0K}^e$ and $\mathcal{H}_{0K}^m$ can be combined in a block-diagonal fashion to write down the unperturbed Hamiltonian acting on the expanded four-component vector $\boldsymbol{V}_K$. The formal expression for the Hamiltonian is $\mathcal{H}_{0K}(\delta\boldsymbol{k}) = v_D\hat{s}_0(\delta k_x\hat{\sigma}_x + \delta k_y\hat{\sigma}_y)$, where the Kronecker product (e.g., $\hat{s}_0\hat{\sigma}_z \equiv \hat{s}_0 \otimes \hat{\sigma}_z$) of 2×2 matrices is used and $\hat{s}_0$ and $\hat{s}_{x,y,z}$ are the unity and Pauli matrices operating on the space of the spin states.

The final basis expansion is achieved by including both the K and K' valleys of the BZ by introducing an eight-component spinor, $\boldsymbol{\Psi} = [\boldsymbol{V}_K; \mathbf{T}\boldsymbol{V}_{K'}]$, where the transformation matrix $\mathbf{T}$ swaps the RCP and LCP orbital states. By introducing the Pauli matrices $\hat{\tau}_{x,y,z}$ and $\hat{\tau}_0$ operating on the valley subspace and using symmetry considerations, the effective 8×8 unperturbed Hamiltonian spanning the orbit, valley, and spin subspaces can be generalized to $\mathcal{H}_0(\delta\boldsymbol{k}) = v_D(\delta k_x\hat{\tau}_z\hat{s}_0\hat{\sigma}_x + \delta k_y\hat{\tau}_0\hat{s}_0\hat{\sigma}_y)$. Here the Kronecker product (e.g., $\hat{\tau}_0\hat{s}_0\hat{\sigma}_z \equiv \hat{\tau}_0 \otimes \hat{s}_0 \otimes \hat{\sigma}_z$) of 2×2 matrices is used, and $\hat{\tau}_0$ and $\hat{\tau}_{x,y,z}$ are the unity and Pauli matrices operating on the valley space. Note that both δk_x and the expected value of $\hat{\tau}_z$ flip sign when operating in the K' valley.

The above obtained unperturbed Hamiltonian $\mathcal{H}_0(\delta\boldsymbol{k})$ is precisely the low-energy Hamiltonian of 2D electron gas in graphene. As the next step, we find the perturbed Hamiltonian $\mathcal{H}(\delta\boldsymbol{k}) = \mathcal{H}_0 + \mathcal{H}_{SOC/T/P}$ that emerges in response to the perturbations of the PhG photonic lattice [shown in Figs. 2(a)–2(c)]. The lowest order perturbation theory neglects the $\delta\boldsymbol{k}$ dependence of $\mathcal{H}_{SOC/T/P}$ and calculates those at $\delta\boldsymbol{k} = 0$ by using the unperturbed fields of the PhG at the edges of the BZ as the expansion basis.

C. Effective Hamiltonians for the three bulk photonic topological phases

Specifically, using the Slater's theory [45] for calculating the eigenfrequencies of a perturbed cavity, as well as the generalization of the Slater's theory [46] that allows for degenerate unperturbed modes, we derive below the expressions for the magnitudes and signs of the bandgap produced by the perturbations of the PhG. Two types of perturbations are considered: (a) those that deform the metallic boundaries of the unit cell, such as the perturbations shown in Figs. 2(a) and 2(c), and (b) those that perturb the material properties of the nonmetallic portions of the unit cell, such as the perturbation shown in Fig. 2(b).

Formally, the electric and magnetic fields $(\boldsymbol{E}', \boldsymbol{H}')$ of the perturbed modes at $\delta\boldsymbol{k} = 0$ are expanded a

$$\boldsymbol{E}' = \sum_n a_n \boldsymbol{E}_n \quad \text{and} \quad \boldsymbol{H}' = \sum_n a_n \boldsymbol{H}_n, \tag{3}$$

where $(\boldsymbol{E}_n, \boldsymbol{H}_n)$ are the $\delta\boldsymbol{k} = 0$ eigenfields of the PhG forming an orthonormal basis, and $a_n s$ represent the degree of hybridization between the unperturbed modes. The generalized Slater matrix is then given by [11,29,48]:

$$\begin{pmatrix} \omega_{11} + \kappa_{11} & \kappa_{12} & \cdots \\ \kappa_{21} & \omega_{22} + \kappa_{22} & \cdots \\ \vdots & \vdots & \ddots \end{pmatrix} \begin{pmatrix} a_1 \\ a_2 \\ \vdots \end{pmatrix} = \omega' \begin{pmatrix} a_1 \\ a_2 \\ \vdots \end{pmatrix}, \tag{4}$$

where ω_{mn}, with $m,n = 1,2,3\cdots$, is the eigenfrequency of the corresponding unperturbed modes; the frequency of the perturbed modes, ω's, are obtained by solving the eigenvalue problem of Eq. (4).

The numerical values of the coupling coefficient,κ_{mn}, depends on the type of a perturbation. For example, for those perturbations that involve inserting metal, the coupling coefficient is given by the following overlap integral,

$$\kappa_{mn} = -\int_{\Delta V} (\omega_m \boldsymbol{E}_m^* \cdot \boldsymbol{E}_n - \omega_n \boldsymbol{H}_m^* \cdot \boldsymbol{H}_n) dV, \tag{5}$$

where ΔV is the perturbed volume where an extra piece of metal is inserted and the eigenfields are normalized as $\int_V (|\boldsymbol{E}_n|^2 + |\boldsymbol{H}_n|^2) dV = 1$, with V being the volume of a unit

cell. When four dipolar modes that degenerate at the Dirac frequency ω_D are hybridized, the following dimensionless coupling strength is defined:

$$\Delta_{mn} \equiv \kappa_{mn}/\omega_{\mathrm{D}} = -\int_{\Delta V} (\boldsymbol{E}_m^* \cdot \boldsymbol{E}_n - \boldsymbol{H}_m^* \cdot \boldsymbol{H}_n) dV. \quad (6)$$

In the case in which the PhG is perturbed by changing its material properties, the basic formulation remains unchanged, except that Eq. (6) is modified according to the standard cavity perturbation theory [49],

$$\Delta_{mn} = -\int_V (\boldsymbol{E}_m^* \cdot \Delta\bar{\bar{\epsilon}} \cdot \boldsymbol{E}_n + \boldsymbol{H}_m^* \cdot \Delta\bar{\bar{\mu}} \cdot \boldsymbol{H}_n)\, dV, \quad (7)$$

where $\Delta\bar{\bar{\epsilon}}$ and $\Delta\bar{\bar{\mu}}$ are the changing permittivity and permeability and ΔV is the region where the material properties are changed. In the next section, we apply the perturbation theory and calculate the coupling strengths in the case of the three PTIs shown in Fig. 2. While some of these perturbative frequency shift calculations can be found in the literature [11,29,33], here we present those derivations for the sake of completeness. We then use the results to formulate the low-energy Hamiltonian of the electromagnetic waves in gapped PhG structures (which now represent PTIs) in the spectral proximity of the Dirac points.

Effective Hamiltonian for the QH-PTI and QVH-PTI. We start with the two perturbations that do not produce TE/TM mode coupling due to the mirror symmetry with respect to the x-y plane. The PhG perturbation shown in Fig. 2(b) results in the QH-PTI. The tripodlike perturbation of the rod's shape shown in Fig. 2(c) results in a QVH-PTI. Note that the rod's shape is chosen to obey the C_3 point group symmetry, which is crucial for preventing intervalley scattering. Because these perturbations do not couple TE and TM modes, the calculation is greatly simplified. Further simplification comes from noting that the perturbed Hamiltonians are diagonalized in the CP basis. This is well known for the gyromagnetic perturbation [33], and we rigorously prove it in the Supplemental Material [50]. For now, we will work under this diagonalization assumption. Therefore, the perturbation Hamiltonians in the K-valley can be written as $\mathcal{H}_{T,K}^{e,m} = \omega_D \Delta_{T,K}^{e,m} \hat{\sigma}_z$ and $\mathcal{H}_{P,K}^{e,m} = \omega_D \Delta_{P,K}^{e,m} \hat{\sigma}_z$ for the QH-PTI and QVH-PTI, respectively. By definition, the perturbed electromagnetic solutions and their eigenfrequencies $\Omega_{P,K}^{e,m}(\delta\boldsymbol{k})$ and $\Omega_{T,K}^{e,m}(\delta\boldsymbol{k})$ for the two types of perturbations are obtained by solving the following equations: $(\mathcal{H}_{0K}^{e,m}(\delta\boldsymbol{k}) + \mathcal{H}_{T,K}^{e,m})\mathbf{U} = \Omega_{T,K}^{e,m}\mathbf{U}$ for the QH-PTI and $(\mathcal{H}_{0K}^{e,m}(\delta\boldsymbol{k}) + \mathcal{H}_{P,K}^{e,m})\mathbf{U} = \Omega_{P,K}^{e,m}\mathbf{U}$ for the QVH-PTI, respectively. The half-bandgap sizes for these two PTIs are defined as follows: $2\Delta_{T,K}^{e(m)} = \Delta_{RR}^{T,e(m)} - \Delta_{LL}^{T,e(m)}$ and $2\Delta_{P,K}^{e(m)} = \Delta_{RR}^{P,e(m)} - \Delta_{LL}^{P,e(m)}$, where

$$\begin{aligned}\Delta_{RR(LL)}^{T,e(m)} &= -\frac{1}{2}\int_{\Delta V_{\mathrm{gap}}} \left(\boldsymbol{h}_{e(m),\perp}^{R(L)*} \cdot \Delta\bar{\bar{\mu}}_{\perp} \cdot \boldsymbol{h}_{e(m),\perp}^{R(L)}\right) dV \\ &= \frac{\delta}{2}\int_{\Delta V_{\mathrm{gap}}} \mathcal{G}_{R(L)}^{e(m)}(\boldsymbol{r}; K)\, dV, \\ \Delta_{RR(LL)}^{P,e(m)} &= -\frac{1}{2}\int_{\Delta V_{\mathrm{ext}}} \left(\boldsymbol{e}_{e(m)}^{R(L)*} \cdot \boldsymbol{e}_{e(m)}^{R(L)} - \boldsymbol{h}_{e(m)}^{R(L)*} \cdot \boldsymbol{h}_{e(m)}^{R(L)}\right) dV \\ &= -\frac{1}{2}\int_{\Delta V_{\mathrm{ext}}} \mathcal{L}_{R(L)}^{e(m)}(\boldsymbol{r}; K)\, dV. \end{aligned} \quad (8)$$

The integrands in the expressions for $\Delta_{RR}^{P,e(m)}$ and $\Delta_{LL}^{P,e(m)}$ (both defined for the electromagnetic fields at the K edge of the BZ) are the Lagrangian densities defined as $\mathcal{L}_R^{e(m)}(\boldsymbol{r}; K) = |\boldsymbol{e}_{e(m)}^R|^2 - |\boldsymbol{h}_{e(m)}^R|^2$ for the RCP orbital state and $\mathcal{L}_L^{e(m)}(\boldsymbol{r}; K) = |\boldsymbol{e}_{e(m)}^L|^2 - |\boldsymbol{h}_{e(m)}^L|^2$ for the LCP orbital state. Likewise, the integrands in the expressions for $\Delta_{RR}^{T,e(m)}$ and $\Delta_{LL}^{T,e(m)}$ are the helicity densities defined as $\mathcal{G}_R^{e(m)}(\boldsymbol{r}; K) = i\hat{z} \cdot [\boldsymbol{h}_{e(m)}^{R*} \times \boldsymbol{h}_{e(m)}^R] +$ c.c. for the RCP and $\mathcal{G}_L^{e(m)}(\boldsymbol{r}; K) = i\hat{z} \cdot [\boldsymbol{h}_{e(m)}^{L*} \times \boldsymbol{h}_{e(m)}^L] +$ c.c. for the LCP states. The integration volume ΔV_{gap} stands for the volume filled with the gyromagnetic material [marked in Fig. 2(b) as red], and the integration volume ΔV_{ext} stands for the metal-filled extruded volume of the tripods [shown in Fig. 2(c)] whose orientation determines the sign (see the Supplemental Material [50]) and the magnitude of $\Delta_{P,K}^{e(m)}$ (for the QVH-PTI). The gap-filling gyromagnetic material is assumed to have the following constitutive parameters: $\epsilon = 1$, $\mu_{xx/yy/zz} = 1$, $\mu_{xy} = -\mu_{yx} = -i\delta$, and $\mu_{ij} = 0$.

Note that the overall frequency shifts experienced by both RCP and LCP states, $2\Gamma_{T,K}^{e(m)} = \Delta_{RR}^{T,e(m)} + \Delta_{LL}^{T,e(m)}$ for the QH-PTI and $2\Gamma_{P,K}^{e(m)} = \Delta_{RR}^{P,e(m)} + \Delta_{LL}^{P,e(m)}$ for the QVH-PTI, are not essential to the topological properties of the PTIs. Therefore, we do not include them in the effective Hamiltonian $\mathcal{H}_K^{e,m}(\delta\boldsymbol{k}) = \mathcal{H}_{0K}^{e,m}(\delta\boldsymbol{k}) + \mathcal{H}_{T/P,K}^{e,m}$. On the other hand, the absolute magnitudes of the bandgap coefficients $|2\Delta_{T,K}^{e(m)}|$ and $|2\Delta_{P,K}^{e(m)}|$ determine the size of the bandgap, while their signs determine which mode (RCP or LCP) at $\delta\boldsymbol{k} = 0$ lies above (or below) the bandgap. We thus conclude that the bandgap coefficients determine the topological bands' order and separation. To estimate the bandgap coefficients $\Delta_{T/P,K}^{e(m)}$ of Eq. (8), and to illustrate how their magnitudes/signs are affected by the perturbations of the shape and material composition, we plot the relevant unperturbed fields of the PhG [the unit cell is shown in Fig. 3(a)] in Figs. 3(b)–3(i).

Specifically, the Lagrangian densities $\mathcal{L}_R^{e(m)}(\boldsymbol{r}_\perp, z = h_0/2; K)$ and $\mathcal{L}_L^{e(m)}(\boldsymbol{r}_\perp, z = h_0/2; K)$ determining $\Delta_{P,K}^{e(m)}$ are separately plotted at the midplane in Figs. 3(b)–3(e). One can see that because strong fields occupy different corners of the hexagonal unit cell, when a tripodlike perturbation, e.g., Fig. 4(b), is applied, $2\Delta_{P,K}^{e(m)} = \Delta_{RR}^{P,e(m)} - \Delta_{LL}^{P,e(m)} \neq 0$. It is also clearly to see that if the opposite perturbation is applied, i.e., Fig. 4(c), the roles of the RCP and LCP states are switched because $\mathcal{L}_R^{e(m)}(\boldsymbol{r}_\perp)$ and $\mathcal{L}_L^{e(m)}(\boldsymbol{r}_\perp)$ are the mirror images of each other with respect to the mirror reflection with respect to the x axis ($y \to -y$). Therefore, $\Delta_{P,K}^{e(m)}$ flips its sign under the following spatial transformations: (i) tripod rotation by 180° ($x \to -x, y \to -y$) and (ii) P inversion, which is the tripod's reflection with respect to the x axis ($x \to x, y \to -y$). Therefore, the bandgap opening requires that the tripods are not invariant under the P inversion. For example, for an inversion-symmetric tripod shown in Fig. 4(a), $\Delta_{RR}^{P,e(m)} = \Delta_{LL}^{P,e(m)}$, and $\Delta_{P,K}^{e(m)}$ vanishes. That means that the RCP and LCP orbital states are degenerate and that the bandgap vanishes. On the other hand, the specific orientations of the tripod in Figs. 4(b) and 4(c) are chosen to maximize the effect of perturbation, i.e.. the magnitude of the bandgap that is proportional to $|\Delta_{P,K}^{e(m)}|$.

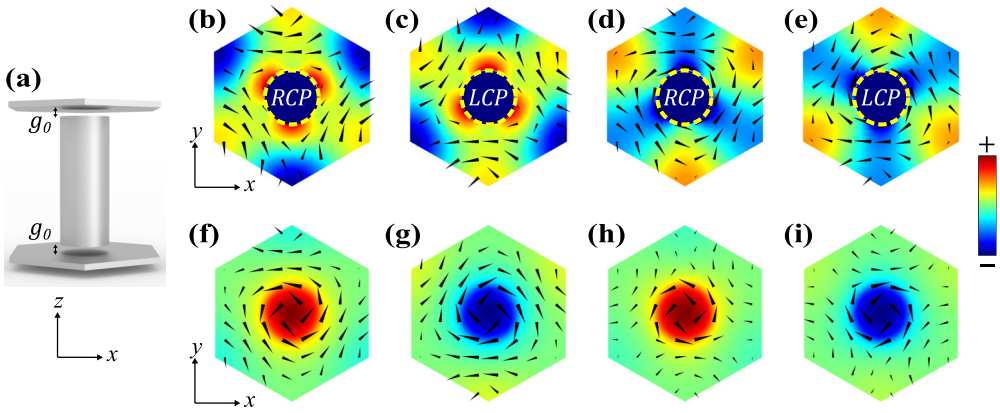

FIG. 3. Overlap fields of the unperturbed PhG. (a) Schematic of the unit cell of the PhG with symmetric gaps. (b), (c) Color-coded TM overlap fields (Lagrangian density) $\mathcal{L}_L^m(\boldsymbol{r}_\perp, z = h_0/2; K) = |\boldsymbol{e}_m^L|^2 - |\boldsymbol{h}_m^L|^2$ for the LCP, and $\mathcal{L}_R^m(\boldsymbol{r}_\perp, z = h_0/2; K) = |\boldsymbol{e}_m^R|^2 - |\boldsymbol{h}_m^R|^2$ for the RCP basis states, respectively. (d), (e) Same as (b) and (c), but for the TE polarization: plots of $\mathcal{L}_L^e(\boldsymbol{r}_\perp, z = h_0/2; K) = |\boldsymbol{e}_e^L|^2 - |\boldsymbol{h}_e^L|^2$ for the LCP, and $\mathcal{L}_R^e(\boldsymbol{r}_\perp, z = h_0/2; K) = |\boldsymbol{e}_e^R|^2 - |\boldsymbol{h}_e^R|^2$ for the RCP basis states, respectively. Arrows: In-plane power flux illustrating the orbital state of the modes. (f)–(i) Same as (b)–(e), but the plotted color-coded quantities are the helicity densities $\mathcal{G}_{R(L)}^{e(m)}(\boldsymbol{r}_\perp, z = g_0/2; K) = i\hat{z} \cdot [\boldsymbol{h}_{e(m)}^{R(L)*} \times \boldsymbol{h}_{e(m)}^{R(L)}] +$ c.c. for all possible orbital and polarization states: $\mathcal{G}_L^m(\boldsymbol{r}_\perp, z = g_0/2; K)$ for the TM-polarized LCP modes in (f), $\mathcal{G}_R^m(\boldsymbol{r}_\perp, z = g_0/2; K)$ for the TM-polarized RCP states in (g), $\mathcal{G}_L^e(\boldsymbol{r}_\perp, z = g_0/2; K)$ for the TE-polarized LCP modes in (h), and $\mathcal{G}_R^e(\boldsymbol{r}_\perp, z = g_0/2; K)$ for the TM-polarized RCP state in (i). Arrows: In-plane power flux illustrating the orbital state of the modes. Physical dimensions of the PhG lattice: $h_0 = a_0$, $d_0 = 0.345a_0$, $g_0 = 0.05a_0$. Lagrangian densities and helicity densities plotted in (b)–(i) correspond to the fields at the K point of the Brillouin zone. Note that the corresponding densities for RCP and LCP states switch at the K' point.

The helicity densities $\mathcal{G}_R^{e(m)}(\boldsymbol{r}_\perp, z = g_0/2; K)$ and $\mathcal{G}_L^{e(m)}(\boldsymbol{r}_\perp z = g_0/2; K)$ determining $\Delta_{T,K}^{e(m)}$ are plotted in Figs. 3(f)–3(i) in the gap between the bottom plate and the circular rod at $z = g_0/2$. From the plots in Figs. 3(f)–3(i) we observe that $\Delta_{LL}^{T,e(m)} = -\Delta_{RR}^{T,e(m)}$ for both TE and TM polarizations. Also, we observe that by reversing the applied magnetic field along the z axis, we reverse the signs of $\Delta_{LL}^{T,e(m)}$ and $\Delta_{RR}^{T,e(m)}$ because the off-diagonal part of the magnetic permeability tensor $\delta \propto B_z$.

While the above overlap integrals are, in general, different for the TE and TM coefficients, it is possible to design a photonic structure that satisfies $\Delta_{T,K}^e = \Delta_{T,K}^m \equiv \Delta_{T,K}$ and $\Delta_{P,K}^e = \Delta_{P,K}^m \equiv \Delta_{P,K}$, as we have done for the specific structures shown in Fig. 2. This is a crucial design feature because it enables the integration of QH-PTIs and QVH-PTIs with the QSH-PTI without losing spin degeneracy. Spin degeneracy in itself is essential for preserving the spin DOF. Spin conservation is particularly important for topological protection of the edge states. For example, interfaces between a QSH-PTI and a QVH-PTI (such as shown in Fig. 5) carry edge states that have the following three quantities locked together: the propagation direction, the spin DOF, and the valley DOF. Spin conservation prevents such TPEWs from backscattering by those perturbations that do not violate spin degeneracy. Those would include the perturbation of the tripods' orientation that results in spatially nonuniform values of $\Delta_{P,K}$, as long as $\Delta_{P,K}^e = \Delta_{P,K}^m \equiv \Delta_{P,K}$ is satisfied.

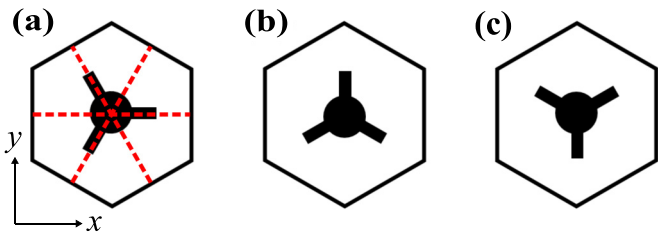

FIG. 4. Three representative unit cells of QVH-PTI. (a) A unit cell with the tips of the tripod pointing along $\Gamma - K(K')$ directions (red dashed lines) that does not break the inversion symmetry. (b), (c) Tripod orientations that maximize the absolute values $|\Delta_P|$ of the bandgap. The signs of Δ_P are opposite for (b) and (c): $\Delta_P < 0$ for (b), and $\Delta_P > 0$ for (c).

Spin degeneracy paves the way to making novel photonic structures containing islands of QVH-PTIs or QH-PTIs embedded in a QSH-PTI matrix. Examples of such devices are shown in Figs. 7 and 8. Spin degeneracy ensures that there are no reflections at the junction points between different photonic phases. Therefore, whenever the spin degeneracy is preserved by design, the effective perturbed Hamiltonians in the K valley assume the following form in the spin states' basis: $\mathcal{H}_{T,K} = \omega_D \Delta_{T,K} \hat{s}_0 \hat{\sigma}_z$ for the gyromagnetic perturbation and $\mathcal{H}_{P,K} = \omega_D \Delta_{P,K} \hat{s}_0 \hat{\sigma}_z$ for the tripod perturbation. These valley-local Hamiltonians are acting on the four-component states $\boldsymbol{V}_K$ defined earlier. At this point, the effective Hamiltonians $\mathcal{H}_{T,K}$ and $\mathcal{H}_{P,K}$ are formally identical. It is only after the valley subspace is included that their properties deviate.

To include both the K and K' valleys of the BZ, we need to use symmetry considerations in order to write down the appropriate Hamiltonian that acts upon the earlier introduced eight-component spinor $\boldsymbol{\Psi} = [\boldsymbol{V}_K; \mathbf{T}\boldsymbol{V}_{K'}]$, where the transformation matrix $\mathbf{T}$ swaps the RCP and LCP orbital states. The mathematical reason (see the Supplemental Material [50] for the derivation details) for the orbital states' swap is that the Lagrangian densities for the RCP (LCP) states at the K point are the same as those for the LCP (RCP) states at the K' point: $\mathcal{L}_{R(L)}^{e(m)}(\boldsymbol{r}; K') = \mathcal{L}_{L(R)}^{e(m)}(\boldsymbol{r}; K)$. On the other hand, helicity densities for the RCP (LCP) states at the K point

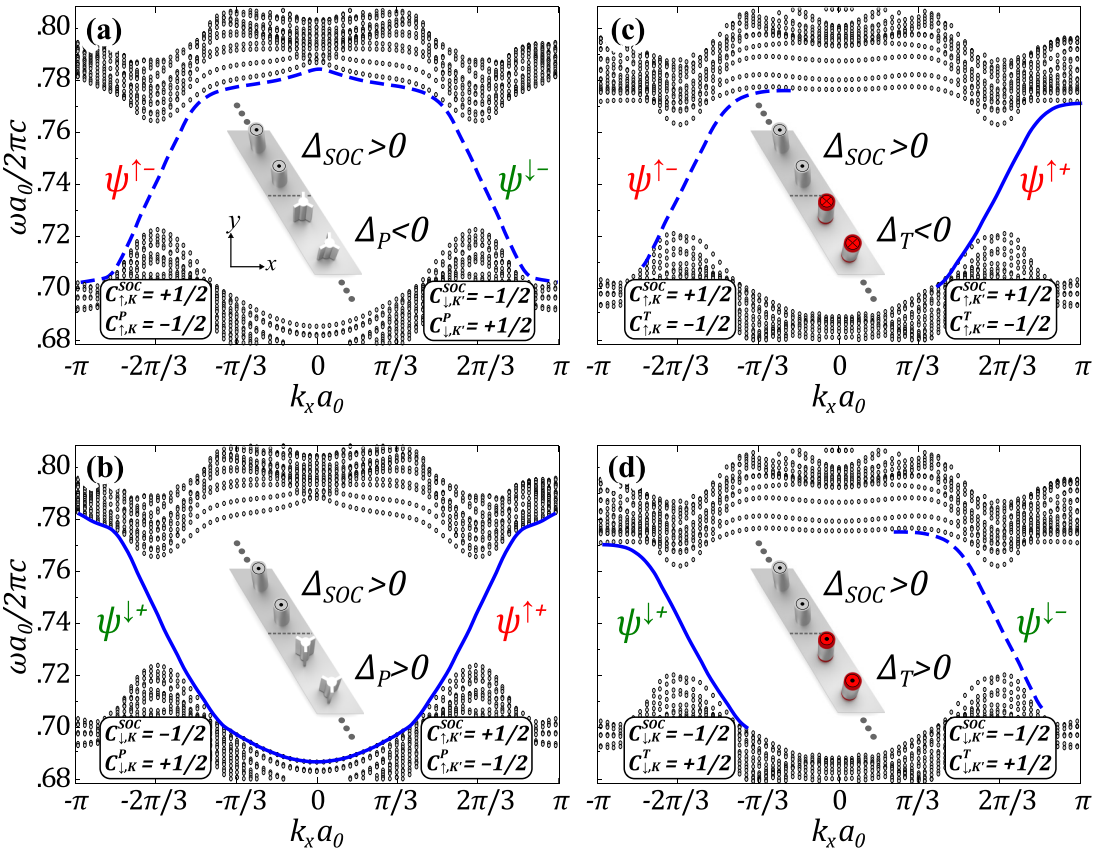

FIG. 5. Topologically protected edge waves (TPEWs) propagating along zigzag-type interfaces between heterogeneous PTI claddings. Photonic band structures of the supercells containing (a), (b) QSH/QVH and (c), (d) QSH/QH PTI interfaces. The supercells contain a single cell along the propagation x direction and 20 cells on each side of the interface. Black circles: bulk modes; blue solid/dashed lines: dispersion curves of the TPEWs with positive/negative $(+/-)$ refractive indices and $\uparrow/\downarrow$ spins. Boxed tags: spin-Chern and valley-Chern numbers of the bulk modes below the bandgap that belong to top/bottom claddings. Due to band-folding, $k_x < 0$ ($k_x > 0$) modes originate from $K(K')$ valleys.

are the opposite of those for the LCP (RCP) states at the K' point: $\mathcal{G}^{e(m)}_{R(L)}(\boldsymbol{r}_\perp; K') = -\mathcal{G}^{e(m)}_{L(R)}(\boldsymbol{r}; K)$. The resulting perturbed Hamiltonians spanning the orbit, spin, and valley subspaces are now given by $\mathcal{H}_T = \omega_D \Delta_T \hat{\tau}_z \hat{s}_0 \hat{\sigma}_z$ and $\mathcal{H}_P = \omega_D \Delta_P \hat{\tau}_0 \hat{s}_0 \hat{\sigma}_z$, where $\hat{\tau}_0$ and $\hat{\tau}_{x,y,z}$ are the unity and Pauli matrices operating on the valley space.

Effective Hamiltonian for the QSH-PTI. Finally, we recall from the earlier work [11] that the perturbed Hamiltonian for the QSH-PTIs formed by the perturbation shown in Fig. 2(a) is given by $\mathcal{H}_{\rm SOC} = \omega_D \Delta_{\rm SOC} \hat{\tau}_z \hat{s}_z \hat{\sigma}_z$, where the value of the bandgap (which can be either positive or negative) is given by the following overlap integral: $\Delta_{\rm SOC} = -1/2 \int_{\Delta V} (\boldsymbol{e}^{R*}_e \cdot \boldsymbol{e}^{R}_m - \boldsymbol{h}^{R*}_e \cdot \boldsymbol{h}^{R}_m - \boldsymbol{e}^{L*}_e \cdot \boldsymbol{e}^{L}_m + \boldsymbol{h}^{L*}_e \cdot \boldsymbol{h}^{L}_m) \quad dV$. Here ΔV is the volume of metal inserted into the gaps between the rods and the plates. Note that $\Delta_{\rm SOC} = 0$ if both gaps are filled. However, when only one of the gaps is filled, as shown in Fig. 2(a), then $\Delta_{\rm SOC} \neq 0$, and the sign of $\Delta_{\rm SOC}$ is determined by which of the two rod-to-plate gaps is filled with metal.

To summarize, the Hamiltonians for the three PTIs shown in Fig. 2 are given by $\mathcal{H}(\delta \boldsymbol{k}) = \mathcal{H}_0 + \mathcal{H}_{{\rm SOC}/T/P}$, where $\mathcal{H}_0 = v_D(\delta k_x \hat{\tau}_z \hat{s}_0 \hat{\sigma}_x + \delta k_y \hat{\tau}_0 \hat{s}_0 \hat{\sigma}_y)$ describes the unperturbed PhG, and

$$\mathcal{H}_{\rm SOC} = \omega_D \Delta_{\rm SOC} \hat{\tau}_z \hat{s}_z \hat{\sigma}_z, \quad \mathcal{H}_T = \omega_D \Delta_T \hat{\tau}_z \hat{s}_0 \hat{\sigma}_z, \quad \mathcal{H}_P = \omega_D \Delta_P \hat{\tau}_0 \hat{s}_0 \hat{\sigma}_z, \tag{9}$$

are the perturbed Hamiltonians of the photonic structures shown in Figs. 2(a)–2(c) respectively.

Equation (9) reveals that these three PTIs are formal photonic counterparts to electronic QSH, QH, and QVH topological insulators, respectively. The topological nature of the propagating spinors $\Psi(\delta \boldsymbol{k})$ satisfying $\mathcal{H}\boldsymbol{\Psi} = \Omega \boldsymbol{\Psi}$ is captured by calculating the appropriate topological indices [28,40,51,52] for each of the three photonic structures.

Specifically, the nonzero spin-Chern and valley-Chern indices exist even in photonic structures with T symmetry that are known to have vanishing total Chern number and can be very useful provided that intervalley and spin-flipping transitions are suppressed [28]. The significance of these additional topological indices for photonics is that they can provide topological protection to surface waves between PTIs with opposing topological indices without breaking the time-reversal symmetry. Therefore, we calculate the local spin-valley indices [53] $C_{s,v} = \int_{{\rm BZ}(v)} d^2\delta \boldsymbol{k}\ [\nabla_{\delta \boldsymbol{k}} \times \boldsymbol{A}(\delta \boldsymbol{k})]_z / 2\pi$, where $s = \uparrow, \downarrow$ is the spin state label, $v = K,\ K'$ is the valley label, and ${\rm BZ}(v)$ is half of the BZ corresponding to $k_x > 0 (<0)$ for $v = K(K')$, respectively. Here the local Berry connection [20,38,39] is $\boldsymbol{A}(\delta \boldsymbol{k}) = -i \boldsymbol{\psi}^{s\dagger}_v(\delta \boldsymbol{k}) \cdot \nabla_{\boldsymbol{k}} \boldsymbol{\psi}^{s}_v(\delta \boldsymbol{k})$, where $\boldsymbol{\psi}^{s}_v(\delta \boldsymbol{k})$ is a projection onto the (s,v) spin-valley subspace of the full spinor $\boldsymbol{\Psi}(\delta \boldsymbol{k})$ propagating below the bandgap. The values of these indices for the Hamiltonians

[given by Eq. (9)] are well known [1,28,40,51–53]. Here we reiterate the values of the Chern $C^T_{s,v}$, spin-Chern $C^{\rm SOC}_{\uparrow/\downarrow,v}$, and valley-Chern $C^P_{s,K/K'}$ numbers in the context of the three photonic structures, shown in Fig. 2:

$$2C^T_{s,v} = \mathrm{sgn}(\Delta_T), \quad 2C^{\rm SOC}_{\uparrow/\downarrow,v} = \pm 1 \times \mathrm{sgn}(\Delta_{\rm SOC}),$$
$$2C^P_{s,K/K'} = \pm 1 \times \mathrm{sgn}(\Delta_P). \tag{10}$$

As expected, only the T-symmetry breaking gyromagnetic structure possesses a nonvanishing *global* Chern number obtained by summing over all spin and valley states. The other Chern numbers can be thought of as *local*, i.e., they are tied to either a specific valley (as is the case for the valley-Chern index $C^P_{s,K/K'}$) or to a specific value of the spin DOF (as is the case for the spin-Chern index $C^{\rm SOC}_{\uparrow/\downarrow,v}$). These local indices impart topological protection to propagating waves for as long as these discrete DOF (valley and/or spin) are conserved due to the specific nature of lattice defects encountered by these waves [11,29]. The numerically calculated propagation bands for the three types of PTIs are plotted in Figs. 2(d)–2(f) and are marked by their corresponding local topological indices. The existence of the local topological indices is crucial because they enable TPEWs between heterogeneous PTIs. The TPEWs emerge because of the impossibility of a continuous interpolation between the band structures across the interface separating two topological phases characterized by different topological indices [17].

IV. THE TPEWs AT THE DOMAIN WALLS BETWEEN HETEROGENEOUS TOPOLOGICAL PHASES

With topological properties of the bulk photonic states of the three PTIs firmly established in Sec. III, we now proceed with presenting the principal finding of this article: the emergence of TPEWs between *heterogeneous* PTIs (shown in Fig. 2). The heterogeneity of the bordering photonic topological phases sets this paper apart from previous works [7,8,11,18,19,29] that dealt with robust photonic edge states between *homogeneous* insulating topological phases. For example, propagation properties of TPEWs at the interfaces between two QSH-PTIs with different topological spin-Chern indices $C^{\rm SOC}_{\uparrow/\downarrow,v}$ were theoretically [7,11] and experimentally [8,18,19] investigated, and their reflectionless nature verified. Likewise, interfaces between two QVH-PTIs with different topological valley-Chern indices $C^P_{s,K/K'}$ were recently theoretically studied [29], and the concept of topological cavities that support TPEWs flowing along such interfaces was introduced. Here we instead concentrate on the interfaces between PTIs of different types, e.g., between QSH-PTI and QVH-PTI.

First, we consider the QSH/QVH interfaces shown in the inset to Figs. 5(a) and 5(b). In the absence of inter-spin and inter-valley scattering, the spin- and valley-locked TPEWs emerge at the interface separating two topological phases characterized by different local Chern indices. From the *bulk-boundary* correspondence principle [28,41,42,28], their number is found as the difference ΔC between topological indices of the top and bottom PTI claddings. Considering a QSH/QVH interface between $\Delta_{\rm SOC} > 0$ and $\Delta_P < 0$ PTIs, we find that $\Delta C = C^{\rm SOC}_{\uparrow,K} - C^P_{\uparrow,K} = 1$ and $\Delta C = C^{\rm SOC}_{\downarrow,K'} - C^P_{\downarrow,K'} = -1$ for K and K' valley states, respectively. Therefore, one spin-up (down) forward (backward)-moving TPEW corresponding to the $K(K')$ valley is supported. This perfect locking between spin and valley DOFs arises because no topologically protected spin-down state in the K valley can exist owing to $C^{\rm SOC}_{\downarrow,K} - C^P_{\downarrow,K} = 0$. This is in contrast with the earlier studied [11] TPEWs at the homogeneous interface between two QSH-like PTIs with opposite signs of the $\Delta_{\rm SOC}$, where both spin states exist in either valley.

The COMSOL band structure calculation indeed reveals the spin-valley locking for the two counter-propagating negative index edge modes [blue dashed lines in Fig. 5(a)] at the valley-preserving [29] zigzag QSH/QVH interface. The simulation was done for a supercell, shown as an inset in Fig. 5(a). The supercell containing a zigzag interface is comprised of one cell in the propagation (x-) direction, and 20 cells of QSH- and QVH-PTIs on either side of the interface. Note that, due to the band-folding effect, the vicinity of the $k_x = 2\pi/3a_0$ point in the supercell's band diagram corresponds to the states of the K' valleys of the bulk QSH- and QVH-PTIs. By reversing the orientation of the tripods [see the inset in Fig. 5(b)] that reverses the sign of Δ_P inside the QVH-PTI cladding, the negative index TPEWs are transformed into the positive index ones [blue solid lines in Fig. 5(b)]. The locking between the spin and the propagation direction is not altered by this change. Instead, the locking between the spin and valley DOFs is changed: For the interface shown in Fig. 5(b), the spin-down state is locked to the K valley, and vice versa.

Next, we consider two examples of QSH/QH interfaces [shown in the insets to Figs. 5(c) and 5(d)]. For a specific value of the magnetic field corresponding to $\Delta_T < 0$ [Fig. 5(c)], this nonreciprocal zigzag interface supports only the forward-propagating TPEWs (solid line: positive; dashed line: negative refractive index), as shown in Fig. 5(c). That is because for either one of the two valleys $\Delta C = 1$ for the spin-up state, but $\Delta C = 0$ for the spin-down state. The energy flow direction of the TPEW is reversed by either changing the sign of the off-diagonal component δ of the magnetic permeability tensor, as can be seen in Fig. 5(d).

Armed with this understanding of the edge states' propagation, we demonstrate how valley-filtering and electromagnetic isolation is accomplished by embedding one topological phase inside another. Below we demonstrate how, by combining these three types of the interfaces between photonic topological phases into an integrated heterogeneous PTI network, different valley and spin DOF can be spatially separated and filtered with nearly perfect efficiency and without reflections. But first, we demonstrate that the conservation of the valley and spin DOF enable reflections-free propagation of TPEWs even when they encounter very large regions of disorder that would normally cause significant backscattering.

V. EXAMPLE 1: ROBUST TRANSPORT OF THE EDGE WAVES THROUGH DISORDERED REGIONS

Topological protection against random disorder is one of the most fascinating properties of the edge states. We have simulated a large defect, which is enclosed by a red box in Fig. 6(a), which is placed in the middle of a QSH-QVH interface. Just as in Fig. 5(a), the QSH-PTI has $\Delta_{\rm SOC} > 0$, the

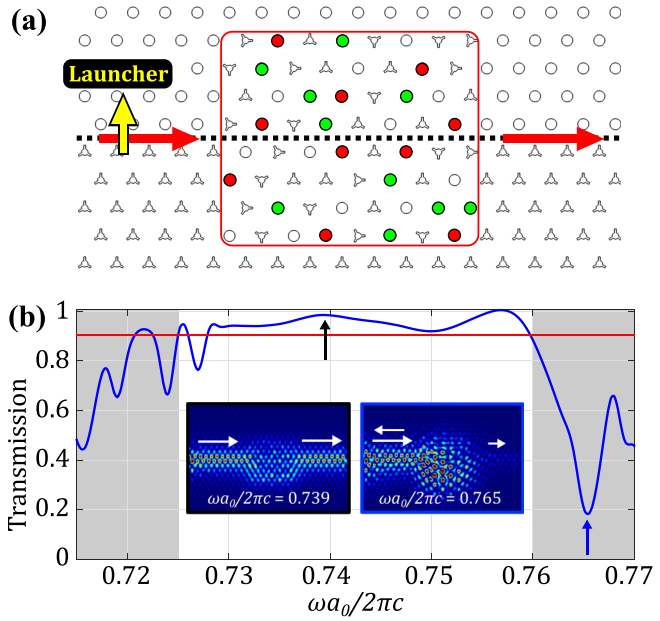

FIG. 6. Topological protected edge wave against a large disordered defect. (a) A disordered defect is an 8×8 array of random unit cells inside the red box. The circles represent QSH-PTI unit cells with the top plate gaps sized at $g_{SOC} = 0.15a_0$ (white), $g_{SOC} = 0.09a_0$ (green), and $g_{SOC} = 0.03a_0$ (red). The tripods represent QVH-PTI unit cells with different orientations. The red arrows indicate the propagation of the TPEW launched along the domain wall between QSH-PTI and QVH-PTI. (b) Transmission spectrum of the TPEW. Red line marks $T = 0.9$ to guide the eye.

QVH-PTI has $\Delta_P < 0$; therefore, forward-propagating spin-up K-valley TPEWs are supported by the domain wall between these two PTIs. The embedded defect has the size of $8a_0 \times 8a_0$, which is much larger than the operational wavelength ($\lambda \approx 1.34a_0$), and can potentially cause significant reflections in the absence of topological protection. The defect consists of a wide variety of unit cells including (i) three different gap sizes of the rods of QSH-PTI unit cells with different values of $\Delta_{SOC} > 0$ and (ii) three different orientations of the tripods of QVH-PTI unit cells with different values (positive and negative) of Δ_P. These different types of unit cells are randomly distributed inside the defect region, as shown in Fig. 6(a). A TPEW arriving at the defect can backscatter if and only if the spin and the valley DOF are flipped upon encountering the defect.

A dipole source placed at the QSH/QVH-PTI interface [as shown in Fig. 6(a)] launches a K-valley edge mode passing through the defect region. The transmission spectrum is shown in Fig. 6(b). One can see that inside the bandgap (unshaded region) the transmission is high ($T > 0.9$ for 87% of the entire bandgap), thereby implying that the TPEWs are not undergoing inter-spin and inter-valley scattering that would scatter them back. The left inset of Fig. 6(b) shows the field distribution for the frequency well inside the bandgap indicated by the black arrow. The transmission is close to unity, and the mode is clearly propagating along the defect's edge.

However, the transmission is significantly decreased when outside the bandgap region because of the scattering of the propagating modes by the defect. The right inset shows the loss of topological protection when operated outside the bandgap at the frequency indicated by the blue arrow. Since this particular QSH-QVH interface [the one shown in Fig. 5(a)] supports a forward-moving spin-up K-valley TPEW and a backward-moving spin-down K'-valley TPEW, the lack of reflection in the disorder test implies that both the valley and spin DOFs are conserved in the topological bandgap.

The conservation of the spin DOF under a limited set of perturbations has been noted earlier [11]. For example, the variation of the gap size g_{SOC} [see Fig. 2(a) for the definition] does not couple the spin-up and spin-down states [11]. Different orientations of the tripods also do not cause inter-spin scattering because of the spin-degeneracy of the QVH-PTI. Likewise, the choice of the tripod-shaped perturbations of the unit cell that satisfies the C_3 rotation symmetry does not cause inter-valley scattering. Thus, the conservation of these DOF ensures that the TPEWs do not backscatter from the disordered defect.

VI. EXAMPLE 2: VALLEY-SORTING OF TPEWs

One of the most intriguing topological effects in condensed matter physics is the possibility of sorting various DOFs (valley, spin, helicity) by applying external fields. For example, valley DOFs can be spatially separated by taking advantage of different Berry curvatures $\Omega_{K(K')} = [\nabla_{\delta k} \times \boldsymbol{A}(\delta \boldsymbol{k})]_z$ experienced by the electrons in the two valleys [23]. It turns out that similar sorting is accomplished for TPEWs when heterogeneous PTIs are interfaced with each other.

The first example shown in Fig. 7(a) is that of a hexagon-shaped QVH-PTI island (comprised of tripod-shaped rods with $\Delta_P < 0$) inside a QSH-PTI sea that contains a zigzag interface between the $\Delta_{SOC} > 0$ (circular rods attached to the top plate) and the $\Delta_{SOC} < 0$ (circular rods attached to the bottom plate) subdomains. The propagation of TPEWs along such interfaces between two topologically distinct QSH-PTIs has been studied in the past [11,18,19]. For readers' convenience, we present the relevant band diagrams and the field profiles of the positive and negative index TPEWs in the Supplemental Material [50]. These TPEWs are impinging from the left onto a topologically-protected polarization-selecting Y-junction formed by the three interfaces at the left-most edge of the hexagon. Our simulations shown in Figs. 7(b) and 7(c) clearly indicate that such a Y-junction can filter the incoming TPEWs according to their valley DOF. Specifically, the QVH-PTI island forms an upper interface shown in the inset of Fig. 5(a), thus guiding the K valley TPEW in the forward direction. On the other hand, the K' valley TPEW must travel along the bottom interface, where the QSH-PTI and QVH-PTI claddings are spatially exchanged, and the signs of the TPEW's valley-Chern are reversed in both claddings. Valley-filtering of a mixed TPEW can then be accomplished by placing an absorber into one of the two halves of the QVH-PTI island.

The above valley-sorting effect is reminiscent of topological currents [24,27,37] that flow in graphene superlattices and inversion asymmetric 2D materials perpendicularly to the applied electric field in the valley-dependent direction. Such separation of the *bulk* valley currents is due to the anomalous velocity $\vec{v}(\vec{k}) \propto \dot{\vec{k}} \times \vec{\Omega}(\vec{k})$ that is caused by the sign change of

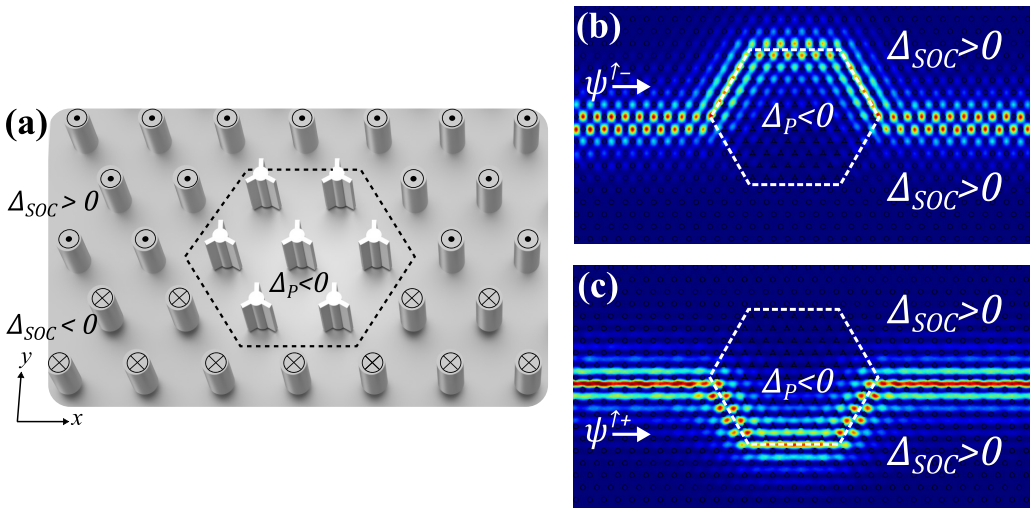

FIG. 7. Valley filtering of TPEWs. (a) Schematic: A QVH-PTI cavity with $\Delta_P < 0$ embedded in a QSH-PTI matrix containing an interface between $\Delta_{SOC} > 0$ (dots) and $\Delta_{SOC} < 0$ (crosses) domains. (b), (c) Valley-dependent deflection of TPEWs launched into the (b) K-valley (negative index) and (c) K'-valley (positive index) modes. The K/K'-valley TPEWs are deflected to the upper/lower arms of the embedded cavity. Color: $|E_z|^2$.

the Berry curvature $\vec{\Omega}(\vec{k})$ between the K and K' valleys. The key difference is that in our case, it is the *edge* state undergoing valley-dependent scattering. Note that valley-selective topologically protected photon transport shown in Figs. 7(b) and 7(c) is enabled by the conservation of the valley DOF. It can be rigorously demonstrated [29] that when the defect's border follows the zigzag trajectory, the inter-valley scattering is identically zero, and full spatial separation of the $K(K')$-valley TPEWs is enabled. Therefore, the convergence point between the three insulating topological phases (QVH-PTI with $\Delta_P < 0$ and QSH-PTIs with $\Delta_{SOC} < 0$ and $\Delta_{SOC} > 0$) forms an ultracompact birefringent Y-junction that routes the photons according to their valley DOF. Such junctions may one day find applications in quantum communications networks and other photonic devices that rely on the entanglement between photons' polarization states.

VII. EXAMPLE 3: A NONRECIPROCAL FOUR-PORT CIRCULATOR

The second example uses QSH- and QH-PTIs to construct a broadband compact four-port circulator [33,34]: a photonic device that nonreciprocally transmits electromagnetic waves from port 1 to port 2. As shown in Fig. 8(a), we construct it by embedding a QH-PTI island inside an interface-containing sea of QSH-PTIs. The interfaces separating the topological phases with different spin-Chern indices support TPEWs with propagation-locked spins labeled by ↑ (red arrows) and ↓ (green arrows). The spin-up TPEWs launched from Port 1 first propagates along the $\Delta_{SOC} > 0/\Delta_{SOC} < 0$ interface between two QSH-PTI domain (input bus waveguide), then merges into the top interface between the QH and QSH PTIs identical to the one in Fig. 5(b), and then passes on to Port 2 without reflections along the output bus waveguide [as shown in Fig. 8(a)]. On

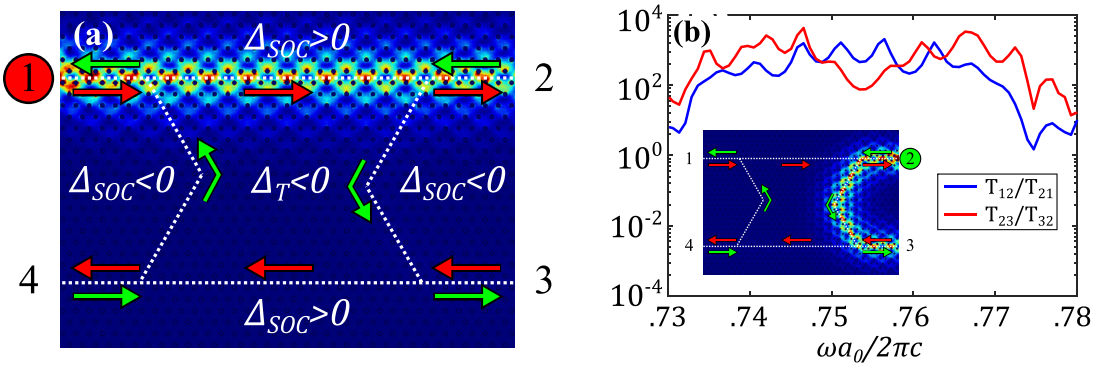

FIG. 8. Four-port circulator based on (a) a QH-PTI cavity with $\Delta_T < 0$ embedded into a QSH-PTI matrix with two domain walls separating the $\Delta_{SOC} < 0$ domain from the $\Delta_{SOC} > 0$ domains. White dashed lines: interfaces between PTIs with indicated signs of Δs. Red (green) arrows: propagation directions of TPEWs with up-spin (down-spin) supported by the interfaces. (a) Energy density profile of TPEW launched from port 1 and heading port 2. (b) The isolation ratio spectra for two different launching ports. Inset: Energy density profile of TPEW launched from port 2 and heading port 3. QSH-PTIs' parameters: $h_0 = a_0$, $d_0 = 0.346a_0$, $g_{SOC} = 0.1a_0$. QH-PTIs' parameters: $h_0 = a_0$, $d_0 = 0.346a_0$, $g_T = 0.05a_0$; gyromagnetic material parameters are the same as Fig. 2(b).

the other hand, the spin-down TPEW launched from Port 2 cannot enter the same top interface because the latter does not support any spin-down edge states, according to Fig. 5(b). Instead of propagating into Port 1, the spin-down state detours into Port 3, as shown in Fig. 8(b). The broadband performance of the device is manifested by large isolation ratios T_{12}/T_{21} (blue solid line) and T_{23}/T_{32}(red solid line) across the entire bandgap plotted in Fig. 8(b).

The above circulator employing only TPEWs has unique advantages over its more conventional photonic counterparts, employing at least some guided modes that are not topologically protected. In general, those devices face considerable challenges in providing broadband performance while retaining small (wavelength-scale) size. For example, using resonant coupling between the topologically trivial bus waveguides and nonreciprocal photonic defect cavity [20,33] results in a narrowband performance for the cavities that are weakly coupled to the input/output waveguides. Increasing the cavity-bus coupling is challenging because of the resulting reciprocal coupling between the waveguides due to their physical proximity [34]. While such coupling can be avoided by using lumped elements, those cannot be used at high frequencies. An alternative approach of using directional coupling between the bus waveguides and one-way (nonreciprocal) waveguides requires elaborate designs to match their propagation constants and coupling strengths over a broad spectral range, as well as a large overall device size (tens of wavelengths) [34]. A comparison with a similarly sized topologically-trivial device is presented in the Supplemental Material [50].

On the contrary, the utilization of TPEWs propagating along the domain walls between multiple PTIs (reciprocal and nonreciprocal) circumvents these problems because the photon routing along the paths shown in Figs. 8(a) and 8(b) is expected to be perfect due to the conservation of the spin. In addition, the nonresonant nature of topologically-protected devices offers significant advantages for high-power operation. The only process setting lower on the device size is the tunneling of the TPEWs between its opposite corners, thus bypassing their prescribed route. The tunneling length $l \propto \Delta^{-1}$ is inversely proportional to the bandgap width Δ. Therefore, this issue becomes less important for even moderately broadband devices. For example, $l \approx a_0$ for the $\Delta/\omega_D \approx 0.07$ design used in the simulations shown in Fig. 8. Note that similar performance could also be achieved by replacing QSH-PTIs with QVH-PTIs.

VIII. CONCLUSIONS

In conclusion, we have identified and designed three types of PTIs that support QSH, QH, and QVH topological phases. Such heterogeneous PTIs can be combined into integrated PTI networks that carry topologically protected electromagnetic edge waves and that can be used in a variety of photonic applications that rely on scattering-free wave propagation: circulators, delay lines, and polarization splitters. Fundamentally, heterogeneous PTIs will enable the emulation of exotic interfaces between electronic topological phases that have been so far challenging to experimentally realize in naturally occurring materials. The three PTIs introduced in this paper provide unique experimental platforms for emulating such heterogeneous interfaces using photons. By introducing nonlinear elements into these photonic platforms, fundamental questions such as the robustness of topological protection to many-body interactions will be experimentally addressed.

ACKNOWLEDGMENTS

This paper was supported by the National Science Foundation (NSF) Award No. PHY-1415547, the Air Force Office of Scientific Research (AFOSR) Grant No. FA9550-15-1-0075, and the Army Research Office (ARO) Grant No. W911NF-16-1-0319.

[1] S. Raghu and F. Haldane, Analogs of quantum-Hall-effect edge states in photonic crystals, Phys. Rev. A **78**, 033834 (2008).
[2] Z. Wang, Y. Chong, J. Joannopoulos, and M. Soljačić, Reflection-Free One-Way Edge Modes in a Gyromagnetic Photonic Crystal, Phys. Rev. Lett. **100**, 013905 (2008).
[3] Z. Wang, Y. Chong, J. D. Joannopoulos, and M. Soljačić, Observation of unidirectional backscattering-immune topological electromagnetic states, Nature **461**, 772 (2009).
[4] M. Hafezi, E. A. Demler, M. D. Lukin, and J. M. Taylor, Robust optical delay lines with topological protection, Nat. Phys. **7**, 907 (2011).
[5] M. Hafezi, S. Mittal, J. Fan, A. Migdall, and J. M. Taylor, Imaging topological edge states in silicon photonics, Nat. Photonics **7**, 1001 (2013).
[6] M. C. Rechtsman, J. M. Zeuner, Y. Plotnik, Y. Lumer, D. Podolsky, F. Dreisow, S. Nolte, M. Segev, and A. Szameit, Photonic Floquet topological insulators, Nature **496**, 196 (2013).
[7] A. B. Khanikaev, S. H. Mousavi, W.-K. Tse, M. Kargarian, A. H. MacDonald, and G. Shvets, Photonic topological insulators, Nat. Mater. **12**, 233 (2013).
[8] W.-J. Chen, S.-J. Jiang, X.-D. Chen, B. Zhu, L. Zhou, J.-W. Dong, and C. T. Chan, Experimental realization of photonic topological insulator in a uniaxial metacrystal waveguide, Nat. Commun. **5**, 5782 (2014).
[9] W. Gao, M. Lawrence, B. Yang, F. Liu, F. Fang, B. Béri, J. Li, and S. Zhang, Topological Photonic Phase in Chiral Hyperbolic Metamaterials, Phys. Rev. Lett. **114**, 037402 (2015).
[10] F. Liu and J. Li, Gauge Field Optics with Anisotropic Media, Phys. Rev. Lett. **114**, 103902 (2015).
[11] T. Ma, A. B. Khanikaev, S. H. Mousavi, and G. Shvets, Guiding Electromagnetic Waves around Sharp Corners: Topologically Protected Photonic Transport in Metawaveguides, Phys. Rev. Lett. **114**, 127401 (2015).
[12] L. Lu, J. Joannopoulos, and M. Soljačić, Topological photonics, Nat. Photonics **8**, 821 (2014).

[13] L.-H. Wu and X. Hu, Scheme for Achieving a Topological Photonic Crystal by Using Dielectric Material, Phys. Rev. Lett. **114**, 223901 (2015).
[14] C. L. Kane and E. J. Mele, Quantum Spin Hall Effect in Graphene, Phys. Rev. Lett. **95**, 226801 (2005).
[15] M. König, S. Wiedmann, C. Brüne, A. Roth, H. Buhmann, L. W. Molenkamp, X.-L. Qi, and S.-C. Zhang, Quantum spin Hall insulator state in HgTe quantum wells, Science **318**, 766 (2007).
[16] B. A. Bernevig and S.-C. Zhang, Quantum Spin Hall Effect, Phys. Rev. Lett. **96**, 106802 (2006).
[17] J. E. Moore, The birth of topological insulators, Nature **464**, 194 (2010).
[18] K. Lai, T. Ma, X. Bo, S. Anlage, and G. Shvets, Experimental realization of a reflections-free compact delay line based on a photonic topological insulator, Sci. Rep. **6**, 28453 (2016).
[19] X. Cheng, C. Jouvaud, X. Ni, S. H. Mousavi, A. Z. Genack, and A. B. Khanikaev, Robust reconfigurable electromagnetic pathways within a photonic topological insulator, Nature Mat. **15**, 542 (2016).
[20] D. J. Thouless, M. Kohmoto, M. P. Nightingale, and M. Den Nijs, Quantized Hall Conductance in a Two-Dimensional Periodic Potential, Phys. Rev. Lett. **49**, 405 (1982).
[21] F. D. M. Haldane, Model for a Quantum Hall Effect without Landau Levels: Condensed-Matter Realization of the "Parity Anomaly", Phys. Rev. Lett. **61**, 2015 (1988).
[22] A. Rycerz, J. Tworzydło, and C. Beenakker, Valley filter and valley valve in graphene, Nat. Phys. **3**, 172 (2007).
[23] D. Xiao, W. Yao, and Q. Niu, Valley-Contrasting Physics in Graphene: Magnetic Moment and Topological Transport, Phys. Rev. Lett. **99**, 236809 (2007).
[24] D. Xiao, M.-C. Chang, and Q. Niu, Berry phase effects on electronic properties, Rev. Mod. Phys. **82**, 1959 (2010).
[25] W. Yao, D. Xiao, and Q. Niu, Valley-dependent optoelectronics from inversion symmetry breaking, Phys. Rev. B **77**, 235406 (2008).
[26] Y. Kim, K. Choi, J. Ihm, and H. Jin, Topological domain walls and quantum valley Hall effects in silicene, Phys. Rev. B **89**, 085429 (2014).
[27] R. V. Gorbachev, J. C. W. Song, G. L. Yu, A. V. Kretinin, F. Withers, Y. Cao, A. Mishchenko, I. V. Grigorieva, K. S. Novoselov, L. S. Levitov, and A. K. Geim, Detecting topological currents in graphene superlattices, Science **346**, 448 (2014).
[28] M. Ezawa, Topological Kirchhoff law and bulk-edge correspondence for valley Chern and spin-valley Chern numbers, Phys. Rev. B **88**, 161406 (2013).
[29] T. Ma and G. Shvets, All-Si valley-Hall photonic topological insulator, N. J. Phys. **18**, 025012 (2016).
[30] W. Yao, S. A. Yang, and Q. Niu, Edge States in Graphene: From Gapped Flat-Band to Gapless Chiral Modes, Phys. Rev. Lett. **102**, 096801 (2009).
[31] J. Jung, F. Zhang, Z. Qiao, and A. MacDonald, Valley-Hall kink and edge states in multilayer graphene, Phys. Rev. B **84**, 075418 (2011).
[32] L. Ju, Z. Shi, N. Nair, Y. Lv, C. Jin, J. Velasco, Jr., C. Ojeda-Aristizabal, H. A. Bechtel, M. C. Martin, A. Zettl, J. Analytis, and F. Wang, Topological valley transport at bilayer graphene domain walls, Nature **520**, 650 (2015).
[33] Z. Wang and S. Fan, Optical circulators in two-dimensional magneto-optical photonic crystals, Opt. Lett. **30**, 1989 (2005).
[34] W. Qiu, Z. Wang, and M. Soljačić, Broadband circulators based on directional coupling of one-way waveguides, Opt. Express **19**, 22248 (2011).
[35] Y. Zhang, T.-T. Tang, C. Girit, Z. Hao, M. C. Martin, A. Zettl, M. F. Crommie, Y. R. Shen, and F. Wang, Direct observation of a widely tunable bandgap in bilayer graphene, Nature **459**, 820 (2009).
[36] D. Xiao, G.-B. Liu, W. Feng, X. Xu, and W. Yao, Coupled Spin and Valley Physics in Monolayers of MoS2 and Other Group-VI Dichalcogenides, Phys. Rev. Lett. **108**, 196802 (2012).
[37] K. F. Mak, K. L. McGill, J. Park, and P. L. McEuen, The valley Hall effect in MoS2 transistors, Science **344**, 1489 (2014).
[38] B. Simon, Holonomy, the Quantum Adiabatic Theorem, and Berry' Phase, Phys. Rev. Lett. **51**, 2167 (1983).
[39] D. Sheng, Z. Weng, L. Sheng, and F. Haldane, Quantum Spin-Hall Effect and Topologically Invariant Chern Numbers, Phys. Rev. Lett. **97**, 036808 (2006).
[40] F. Zhang, A. H. MacDonald, and E. J. Mele, Valley Chern numbers and boundary modes in gapped bilayer graphene, Proc. Natl. Acad. Sci. **110**, 10546 (2013).
[41] M. Z. Hasan and C. L. Kane, Topological insulators, Rev. Mod. Phys. **82**, 3045 (2010).
[42] R. S. Mong and V. Shivamoggi, Edge states and the bulk-boundary correspondence in Dirac Hamiltonians, Phys. Rev. B **83**, 125109 (2011).
[43] B. Xiao, K. Lai, Y. Yu, T. Ma, G. Shvets, and S. M. Anlage, Exciting reflectionless unidirectional edge modes in a reciprocal photonic topological insulator medium, Phys. Rev. B **94**, 195427 (2016).
[44] A. Szameit, M. C. Rechtsman, O. Bahat-Treidel, and M. Segev, PT-symmetry in honeycomb photonic lattices, Phys. Rev. A **84**, 021806(R) (2011).
[45] J. C. Slater, Microwave electronics, Rev. Mod. Phys. **18**, 441 (1946).
[46] G. E. Dombrowski, Matrix formulation of Slater's cavity perturbation theorem, J. Appl. Phys. **55**, 2648 (1984).
[47] D. Malterre, B. Kierren, Y. Fagot-Revurat, C. Didiot, F. J. G. de Abajo, F. Schiller, J. Cordón, and J. E. Ortega, Symmetry breaking and gap opening in two-dimensional hexagonal lattices, New J. Phys. **13**, 013026 (2011).
[48] N. Arju, T. M. Ma, A. Khanikaev, D. Purtseladze, and G. Shvets, Optical Realization of Double-Continuum Fano Interference and Coherent Control in Plasmonic Metasurfaces, Phys. Rev. Lett. **114**, 237403 (2015).
[49] D. M. Pozar, *Microwave Engineering*, 4th ed. (Wiley Global Education, Oak Brook, IL, 2011).
[50] See Supplemental Material at http://link.aps.org/supplemental/10.1103/PhysRevB.95.165102 for additional analytic details and examples.
[51] J. Li, A. F. Morpurgo, M. Büttiker, and I. Martin, Marginality of bulk-edge correspondence for single-valley Hamiltonians, Phys. Rev. B **82**, 245404 (2010).
[52] F. Zhang, J. Jung, G. A. Fiete, Q. Niu, and A. H. MacDonald, Spontaneous Quantum Hall States in Chirally Stacked Few-Layer Graphene Systems, Phys. Rev. Lett. **106**, 156801 (2011).
[53] Y. Yang, Z. Xu, L. Sheng, B. Wang, D. Y. Xing, and D. N. Sheng, Time-Reversal-Symmetry-Broken Quantum Spin Hall Effect, Phys. Rev. Lett. **107**, 066602 (2011).